Supplementary Information

Origin of V_{OC} in Perovskite Solar Cells by Faradaic Junction Model

Mengfan Xue[1†], Zhoujun Li[1†], Qiong Wang[1†], Yihong Chen[2], Jun Luo[2], Ruotong Bao[1], Dongjian Jiang[2], Shengyao Wang[3], Bing Wang[1], Tao Yu[1], Yingfang Yao[2], Wenjun Luo[2*], Zhigang Zou[1,2]

[1]Eco-materials and Renewable Energy Research Center (ERERC), Jiangsu Key Laboratory for Nano Technology, National Laboratory of Solid State Microstructures and Department of Physics, Nanjing University, Nanjing 210093, China

[2]National Laboratory of Solid State Microstructures, College of Engineering and Applied Sciences, Nanjing University, Nanjing 210093, China

[3]School of Chemistry and Chemical Engineering, Shanghai Jiao Tong University, Shanghai 200240, China

[†]These authors contributed equally to this work.

*Email: wjluo@nju.edu.cn;

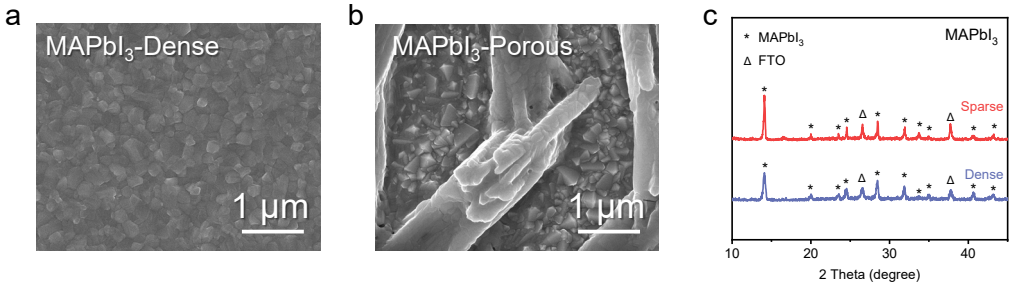

Figure S1. SEM images of dense (a) and sparse (b) $MAPbI_3$; (c) XRD patterns of dense and sparse $MAPbI_3$.

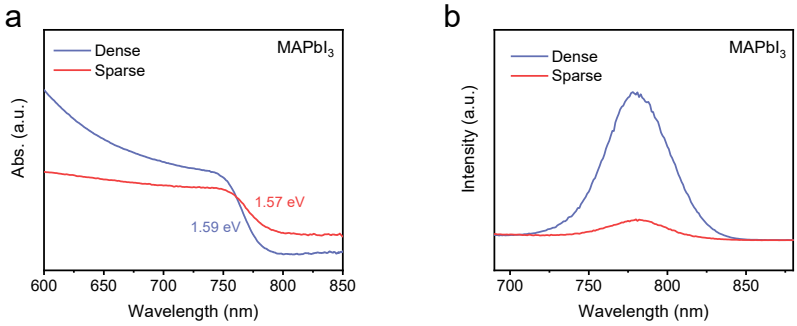

Figure S2. UV-Vis spectra (a) and PL spectra (b) of dense and sparse $MAPbI_3$.

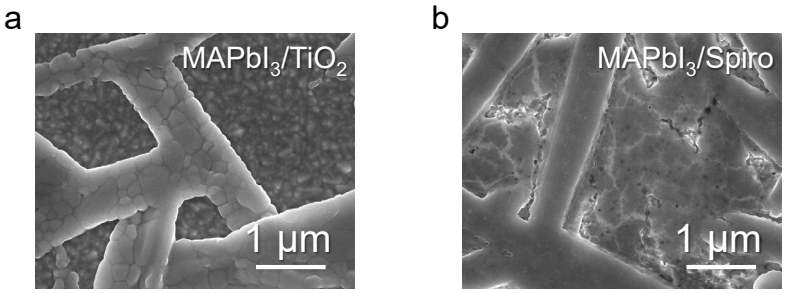

Figure S3. SEM images of $MAPbI_3/TiO_2$ (a) and $MAPbI_3$/Spiro-OMeTAD (b).

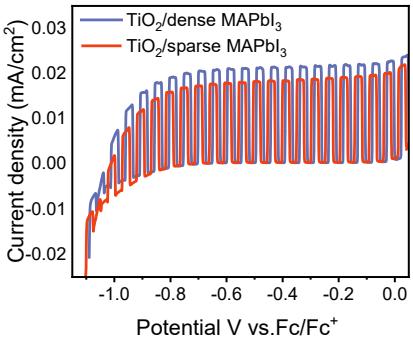

Figure S4. Linear sweep voltammetry (LSV) curves of TiO_2/dense $MAPbI_3$ and TiO_2/sparse $MAPbI_3$ under chopped illumination, electrolyte: 0.1M n-Bu_4NPF_6 in CH_2Cl_2.

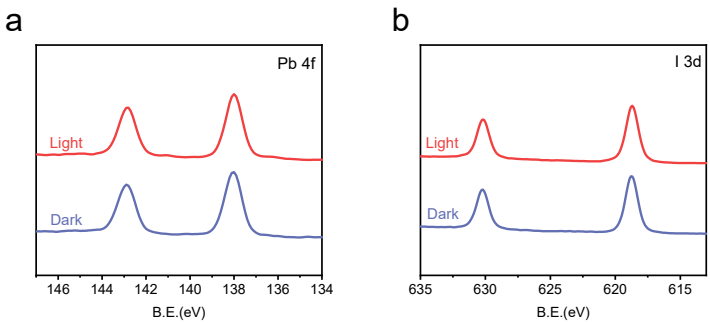

Figure S5. In situ XPS spectra of Pb 4f (a) and I 3d (b) of sparse $MAPbI_3$ in the dark and under illumination.

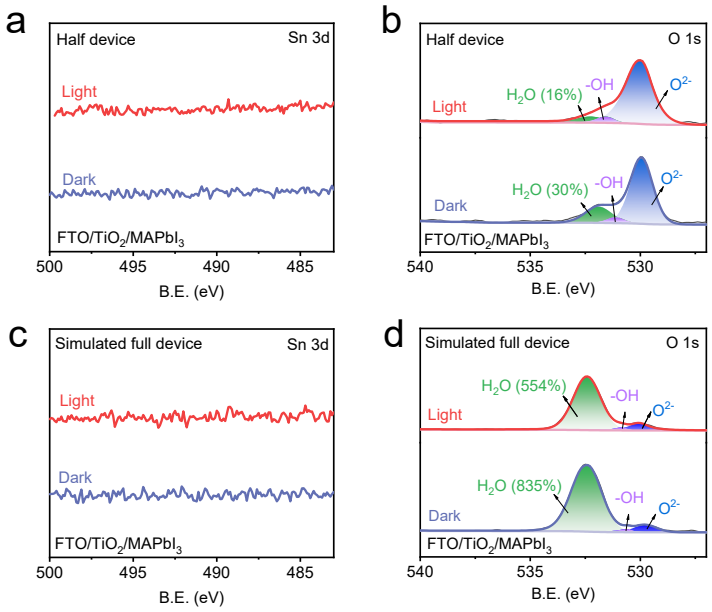

Figure S6. In situ XPS spectra of Sn 3d (a), O 1s (b) and I 3d (c) in a $MAPbI_3/TiO_2$ half device in the dark and under illumination; in situ XPS spectra of Sn 3d (d), O 1s (e) and I 3d (f) in a $MAPbI_3/TiO_2$ half device connected with a $MAPbI_3$/Spiro-OMeTAD half device in the dark and under illumination.

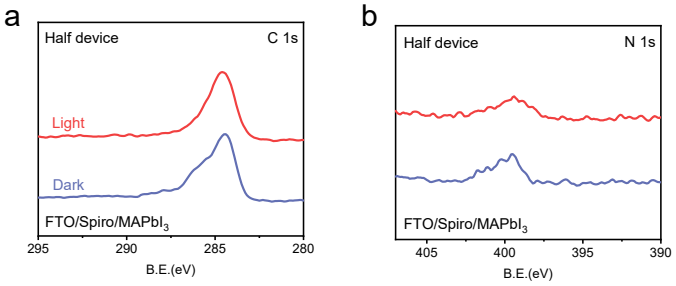

Figure S7. In situ XPS spectra of C 1s (a) and N 1s (b) in $MAPbI_3$/Spiro-OMeTAD in the dark and under illumination.

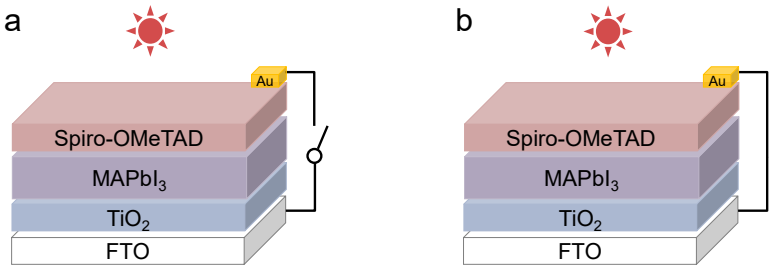

Figure S8. Schematic diagrams of $FTO/TiO_2/MAPbI_3$/Spiro-OMeTAD in open circuit

(a) and short circuit (b) conditions under illumination for in situ FTIR measurement.

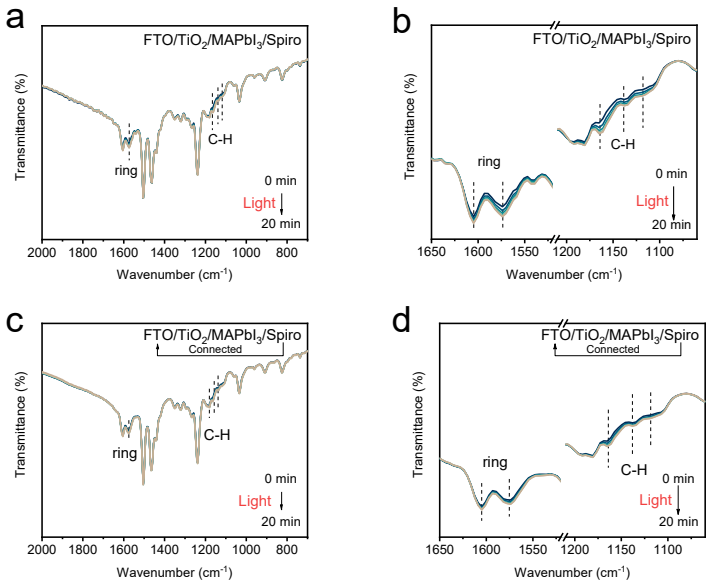

Figure S9. In situ FTIR spectra of FTO/TiO_2/$MAPbI_3$/Spiro-OMeTAD in the dark and under illumination in open circuit conditions (a) and its enlarged area (b); in short circuit conditions (c) and its enlarged area (d).

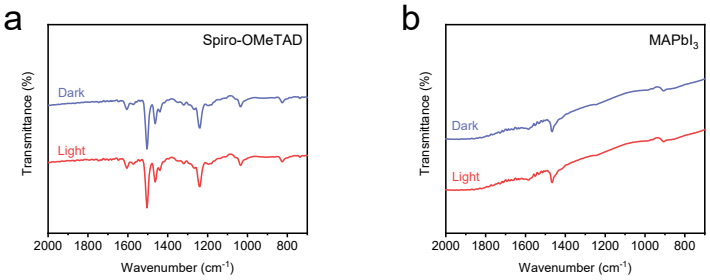

Figure S10. In situ FTIR spectra of FTO/Spiro-OMeTAD (a) and FTO/$MAPbI_3$ (b) in the dark and under illumination for 20 min.

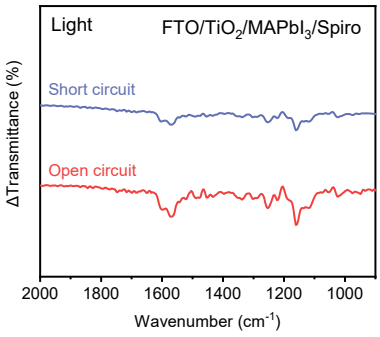

Figure S11. The changes of in situ FTIR spectra of FTO/TiO_2/$MAPbI_3$/Spiro-

OMeTAD/Au before and after illumination for 20 min in open circuit and short circuit conditions.

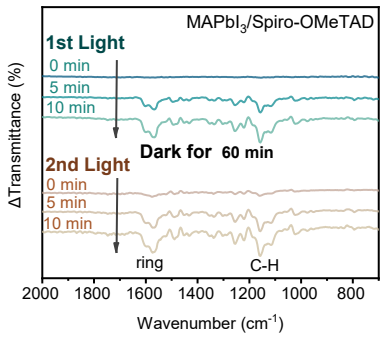

Figure S12. The changes of in situ FTIR spectra of $MAPbI_3$/Spiro-OMeTAD in the dark and under illumination.

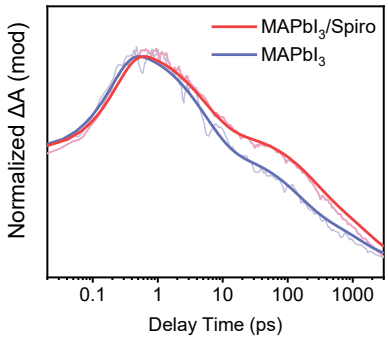

Figure S13. Kinetic traces of $MAPbI_3$ and $MAPbI_3$/Spiro-OMeTAD at 6369 nm. Both films were excited with a laser pulse of 700 nm and a fluence of 246 μJ cm^{-2}. Spiro-OMeTAD is abbreviated as Spiro in the Figure.

Table S1: Time coefficients of $MAPbI_3$ and $MAPbI_3$/Spiro-OMeTAD of kinetic traces at 6369 nm by exponential fitting.

	τ1 (ps)	τ2 (ps)	τ3 (ps)
$MAPbI_3$/Spiro	5.1	210.0	1633.0
$MAPbI_3$	5.2	131.0	1261.0

Considering that charge transfer rate is an important factor that affect the interface charge transfer process, we also measured the fs-TAS of $MAPbI_3$ and $MAPbI_3$/Spiro-OMeTAD to further investigate the charge transfer time in perovskite solar cells, and the kinetic traces are shown in Figure S13. The fit analysis of the two films is shown in Table S1. While τ1 is carrier relaxation lifetime of photo-generated carriers in the $MAPbI_3$, τ2 is the lifetime of surface trapping by the redox chemical reaction of $2I^- + 2h^+ \rightarrow I_2^*$ (* means the excited state) and τ3 is the lifetime of I_2^*. τ1 in the two samples is similar, but τ2 and τ3 in the $MAPbI_3$/Spiro-OMeTAD are higher than that in the pure $MAPbI_3$, which suggest the longer lifetime of surface trapping and I_2^*. The redox chemical reaction process of $2I^- + 2h^+ \rightarrow I_2^*$ is hundreds of ps, which is close to the value in the previous study[1]. Therefore, this faradaic junction charge transfer is very rapid when current flows.

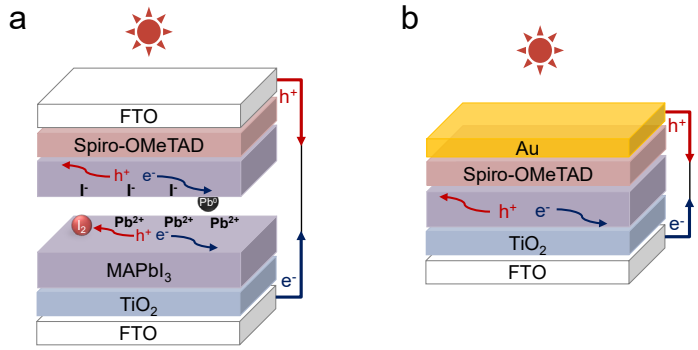

Figure S14. Schematic diagrams of charger transfer processes in the simulated full device (a) and the real full device (b).

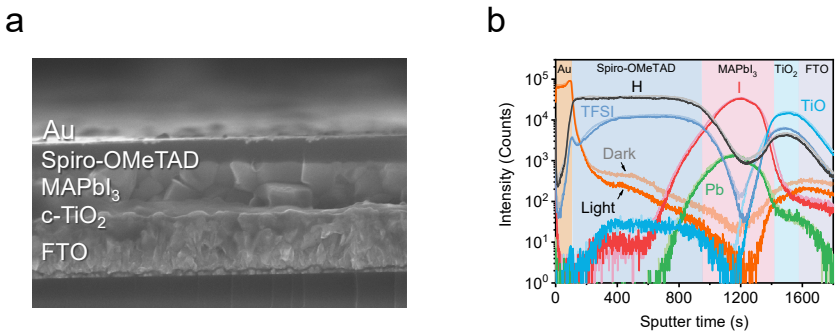

Figure S15. (a) Cross-section SEM image of a full device of FTO/TiO_2/$MAPbI_3$/Spiro-OMeTAD/Au; (b) TOF-SIMS spectra of FTO/TiO_2/$MAPbI_3$/Spiro-OMeTAD/Au in

open circuit condition before and after illumination for 30 min.

The cross-section SEM image of a typical perovskite solar cell of FTO/TiO_2/$MAPbI_3$/Spiro-OMeTAD/Au is shown in Figure S15a. TOF-SIMS was also used to investigate ion distribution in a perovskite solar cell with different depths before and after illumination in open circuit condition and the results are shown in Figure S15b. By TOF-SIMS, the ion distribution in a solar cell is similar before and after illumination. Therefore, the ion migration distance under illumination in open circuit condition is possibly very short at the interface, which is hard to be detected.

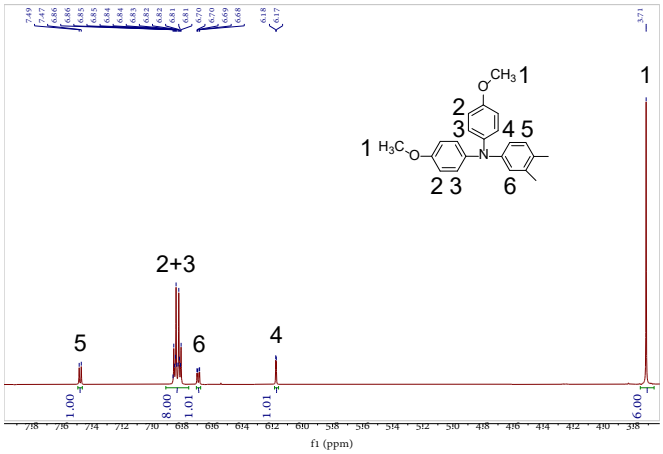

Figure S16. ^{1}H NMR spectra of Spiro-OMeTAD powder (DMSO-d6, 400MHz).

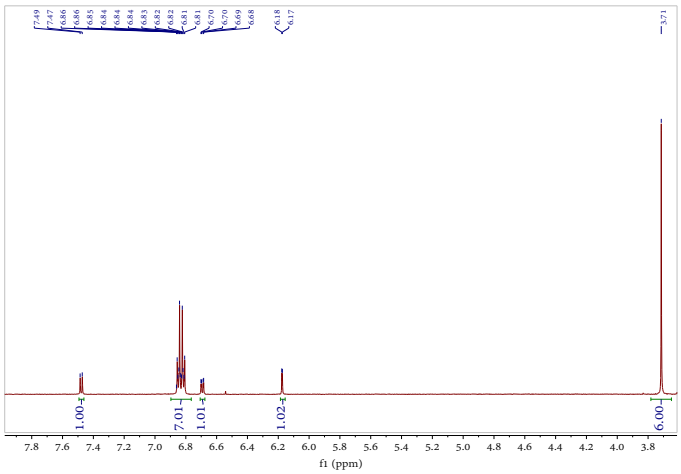

Figure S17. ^{1}H NMR spectra of Spiro-OMeTAD powder after exposure to I_2 vapor for 5 min in the dark (DMSO-d6, 400MHz).

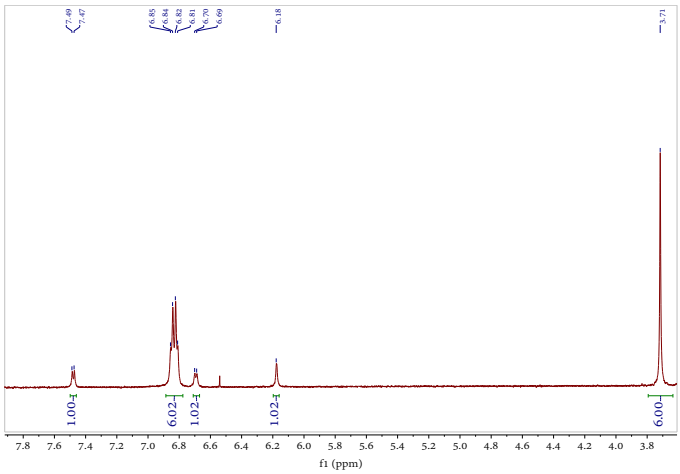

109

110 Figure S18. ^{1}H NMR spectra of Spiro-OMeTAD powder after exposure to I_2 vapor for

111 10 min in the dark (DMSO-d6, 400MHz).

112

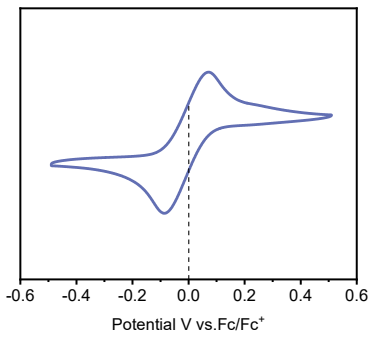

113

114 Figure S19. The CV curve of Pt wire in the electrolyte of 1 mM ferrocene and 0.1 M n-

115 Bu_4NPF_6 in CH_2Cl_2.

116

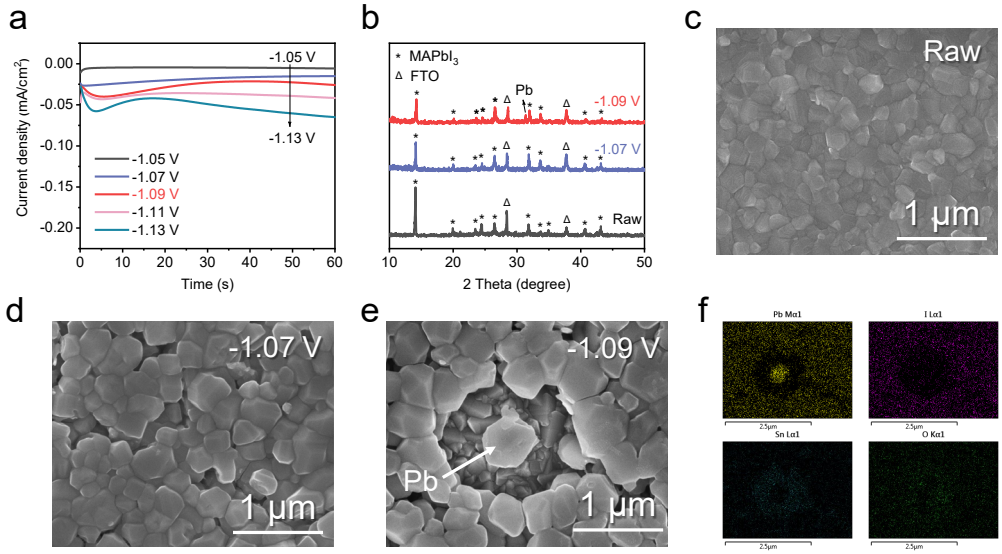

117

118 Figure S20. (a) I-t curves of $MAPbI_3$ at different reduction potentials (b) in the
119 electrolyte of 0.1 M n-Bu_4NPF_6 in CH_2Cl_2; (b) XRD patterns of raw $MAPbI_3$, $MAPbI_3$
120 at -1.07 V and -1.09 V vs. Fc/Fc^+; SEM images of raw $MAPbI_3$ (c), $MAPbI_3$ after
121 electrochemical measurement at -1.07 V (d) and -1.09 V vs. Fc/Fc^+ (e); (f) EDS
122 mapping of $MAPbI_3$ after electrochemical measurement at -1.09 V vs. Fc/Fc^+.

123

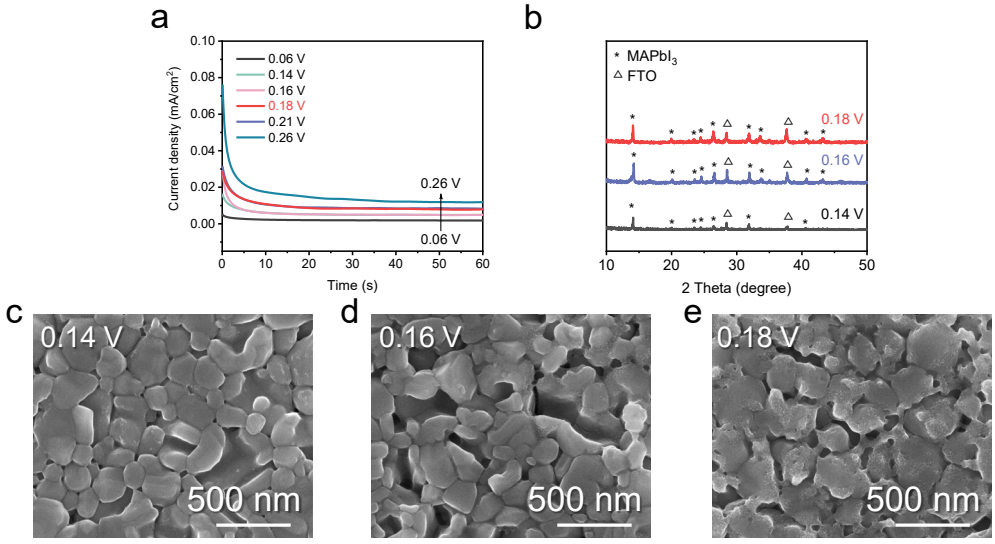

124

125 Figure S21. (a) I-t curves of $MAPbI_3$ at different oxidation potentials (b) in the
126 electrolyte of 0.1 M n-Bu_4NPF_6 in CH_2Cl_2; (b) XRD patterns of $MAPbI_3$ after
127 electrochemical measurement at 0.14 V, 0.16 V and 0.18 V vs. Fc/Fc^+; SEM images of
128 $MAPbI_3$ after electrochemical measurement at 0.14 V(c), 0.16 V (d) and 0.18 V (e) vs.
129 Fc/Fc^+.

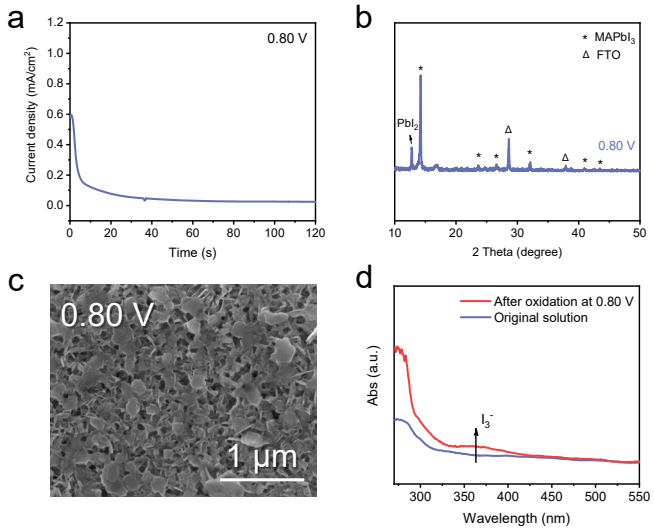

Figure S22. (a) I-t curve of $MAPbI_3$ at 0.80 V vs. Fc/Fc^+ in the electrolyte of 0.1 M n-Bu_4NPF_6 in CH_2Cl_2; the XRD pattern (b) and SEM image (c) of $MAPbI_3$ after electrochemical measurement at 0.80 V vs. Fc/Fc^+; (d) UV-Vis spectra of the electrolytes before and after electrochemical measurement of $MAPbI_3$ at 0.80 V vs. Fc/Fc^+.

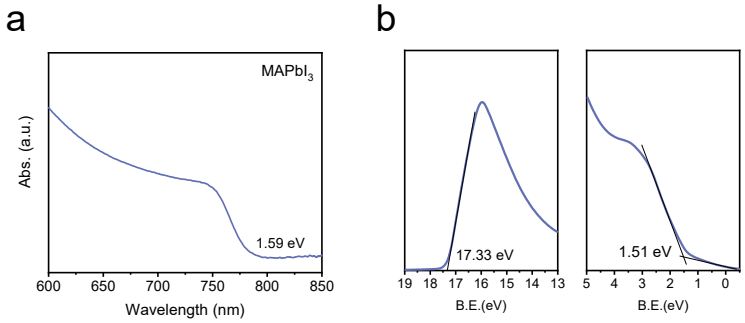

Figure S23. UV-Vis spectra (a) and UPS spectra (b) of $MAPbI_3$.

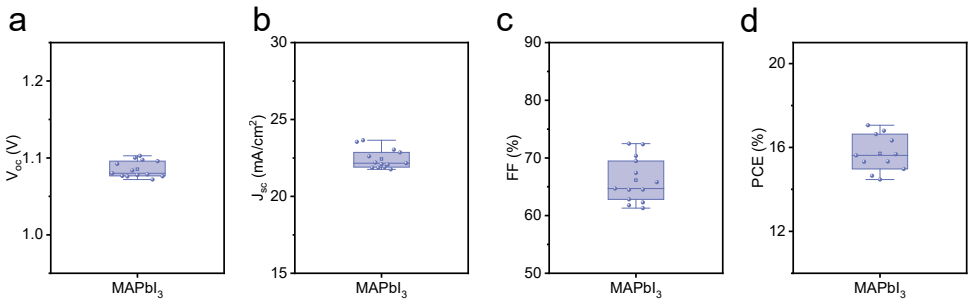

Figure S24. Statistics of V_{OC} (a), J_{SC} (b), FF (c) and PCE (d) of $MAPbI_3$ solar cells.

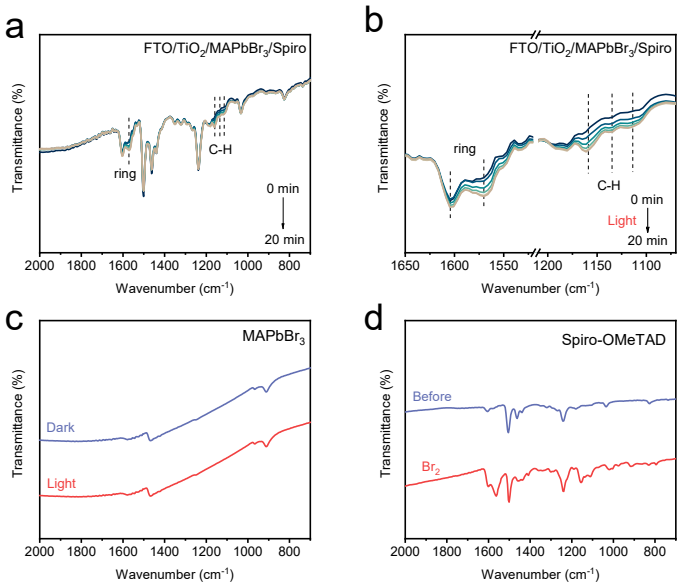

141

142 Figure S25. In situ FTIR spectra of FTO/TiO_2/$MAPbBr_3$/Spiro-OMeTAD in the dark
143 and under illumination in open circuit conditions (a) and its enlarged area (b); (c) FTIR
144 spectra of $MAPbBr_3$ in the dark and under illumination for 20 min; (d) FTIR spectra of
145 Spiro-OMeTAD before and after the exposure to Br_2 for 1 h.

146

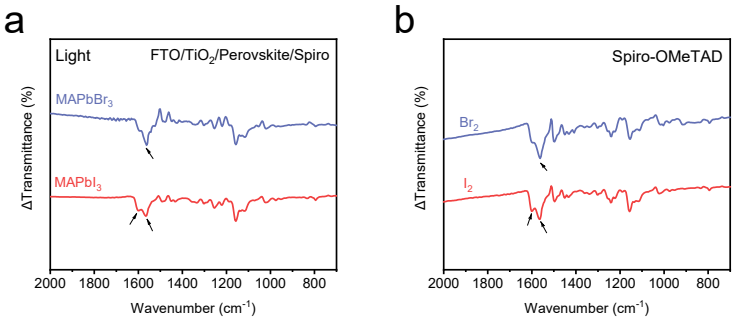

147

148 Figure S26. (a) The changes of in-situ FTIR spectra of FTO/TiO_2/$MAPbI_3$/Spiro-
149 OMeTAD and FTO/TiO_2/$MAPbBr_3$/Spiro-OMeTAD in the dark and under illumination
150 of 20 min; (b) the changes of FTIR spectra of Spiro-OMeTAD before and after the
151 exposure to I_2 for 30 s and Br_2 for 1 h in the dark.

152

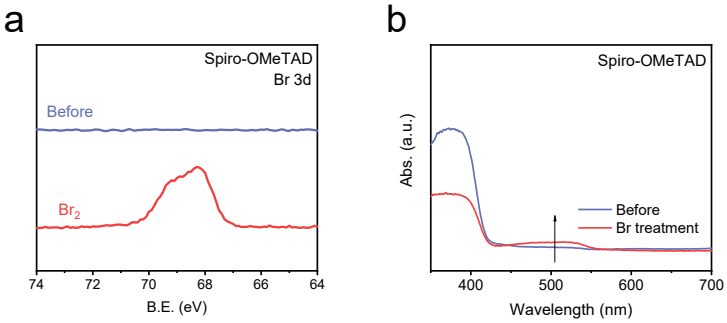

153

154 Figure S27. XPS spectra of Br 3d (a) and UV-Vis spectra (b) of FTO/Spiro-OMeTAD
155 before and after the exposure to Br_2 in the dark.

156

157 To further confirm the universality of the faradic junction model in other wide
158 bandgap perovskite solar cells, interface charge transfer processes in $MAPbBr_3$ solar
159 cells were also investigated by in situ FTIR, XPS and UV-Vis and the results are shown
160 in Figure S25-S27, respectively. Similar to in $MAPbI_3$ solar cells, in situ FTIR spectra
161 of the FTO/TiO_2/$MAPbBr_3$/Spiro-OMeTAD suggest that the stronger peaks of benzene
162 ring and new peaks of C-H under illumination come from oxidation of Spiro-OMeTAD
163 (Figure S25a and S25b). However, the FTIR peaks do not changes on single $MAPbBr_3$
164 under illumination (Figure S25c), and Spiro-OMeTAD can be oxidized by Br_2 in the
165 dark (Figure S25d). Therefore, the oxidation of Spiro-OMeTAD in
166 FTO/TiO_2/$MAPbBr_3$/Spiro-OMeTAD comes from Br_2 on the surface of $MAPbBr_3$
167 under illumination. Different from the results in $MAPbI_3$ solar cells, the peaks of
168 benzene ring indicate a stronger increase at the lower wavenumber of 1566 cm^{-1} (Figure
169 S26). Moreover, XPS and UV-Vis spectra suggest that the existence of Br^- in Spiro-
170 OMeTAD exposed in Br_2 vapor in the dark, which comes from the oxidation of Spiro-
171 OMeTAD (Figure S27).

172

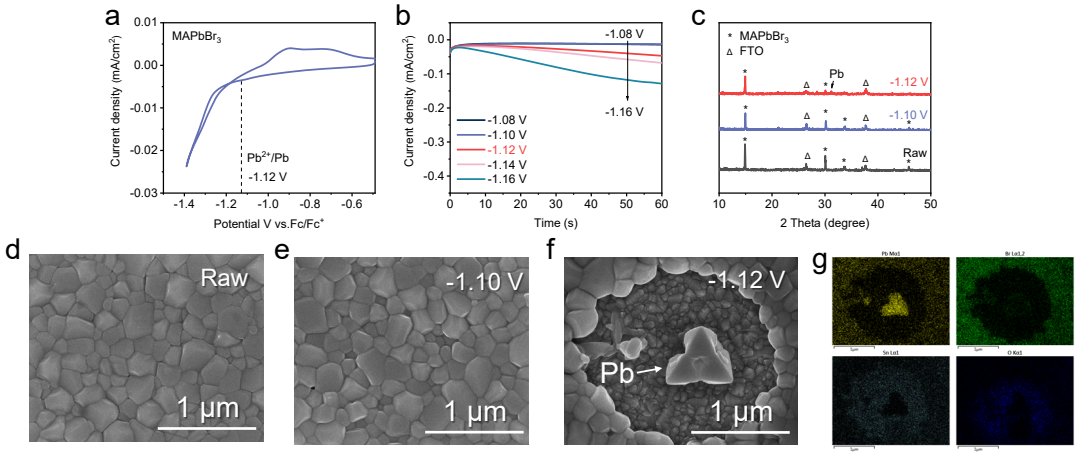

173

174 Figure S28. CV curves (a) and i-t curves of $MAPbBr_3$ at different reduction potentials
175 (b) in the electrolyte of 0.1M n-Bu_4NPF_6 in CH_2Cl_2; (c) XRD patterns of raw $MAPbBr_3$,
176 $MAPbBr_3$ after electrochemical measurement at -1.10 V and -1.12 V vs. Fc/Fc^+; SEM
177 images of raw $MAPbBr_3$ (d), $MAPbBr_3$ after electrochemical measurement at -1.10 V
178 (e) and -1.12 V (f) vs. Fc/Fc^+; (g) EDS mapping of $MAPbBr_3$ after electrochemical
179 measurement at -1.10 V vs. Fc/Fc^+.

180

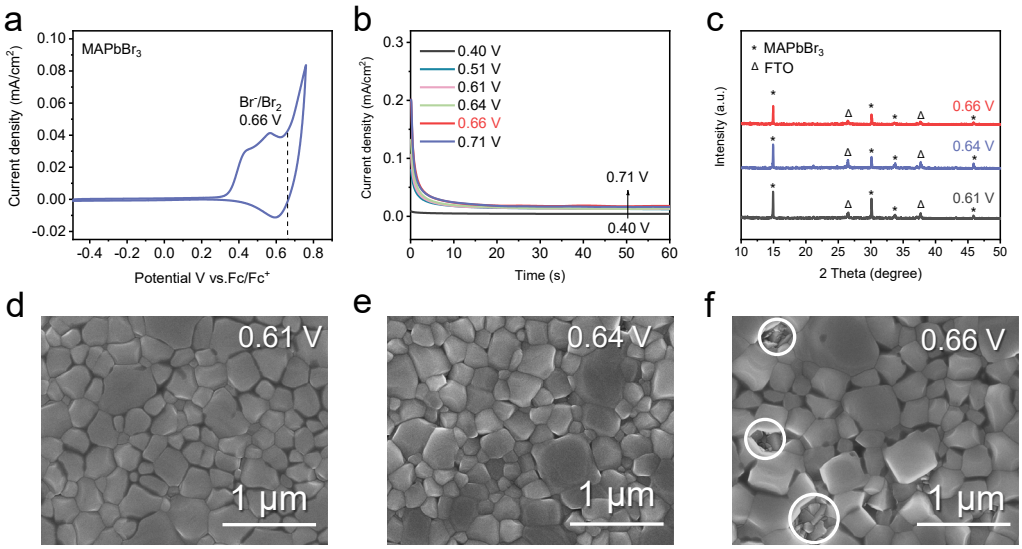

181

182 Figure S29. CV curves (a) and i-t curves of $MAPbBr_3$ at different oxidation potentials
183 (b) in the electrolyte of 0.1M n-Bu_4NPF_6 in CH_2Cl_2; (c) XRD patterns of $MAPbBr_3$
184 after electrochemical measurement at 0.61 V, 0.64 V and 0.66 V vs. Fc/Fc^+; SEM
185 images of $MAPbBr_3$ after electrochemical measurement at 0.61 V (d), 0.64 V (e) and
186 0.66 V (f) vs. Fc/Fc^+. The oxidation corrosion of $MAPbBr_3$ at 0.66 V vs. Fc/Fc^+ is

observed and the FTO substrate is exposed in the areas with white circles.

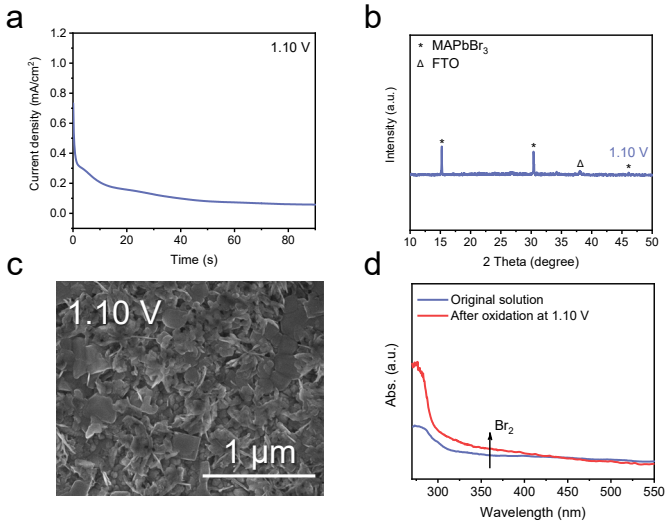

Figure S30. (a) I-t curve of $MAPbBr_3$ at 1.10 V in the electrolyte of 0.1 M n-Bu_4NPF_6 in CH_2Cl_2; the XRD pattern (b) and SEM image (c) of $MAPbBr_3$ after electrochemical measurement at 1.10 V vs. Fc/Fc^+; (d) UV-Vis spectra of electrolytes before and after electrochemical measurement of $MAPbBr_3$ at 1.10 V vs. Fc/Fc^+.

Similar to $MAPbI_3$, the electrochemical reduction and oxidation potentials of $MAPbBr_3$ were measured by CV curves and i-t curves (Figure S28-S30). When the potential is negative than -1.12 V vs. Fc/Fc^+, $MAPbBr_3$ is irreversibly reduced into Pb^0 (Figure S28). When the potential is positive than 0.66 V vs. Fc/Fc^+, $MAPbBr_3$ is irreversibly oxidized into Br_2 (Figure S29 and S30). Therefore, the onset reduction corrosion potential and oxidation corrosion potential of $MAPbBr_3$ is -1.12 V and 0.66 V vs. Fc/Fc^+, respectively.

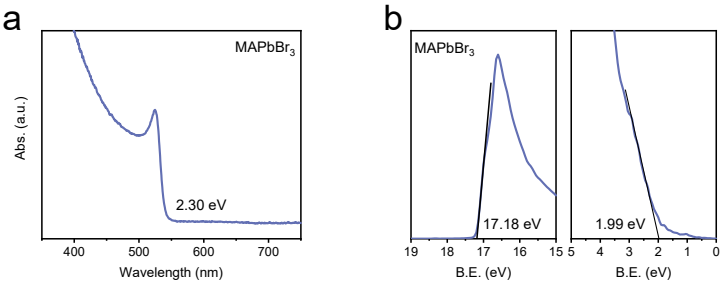

Figure S31. UV-Vis spectra (a) and UPS spectra (b) of $MAPbBr_3$.

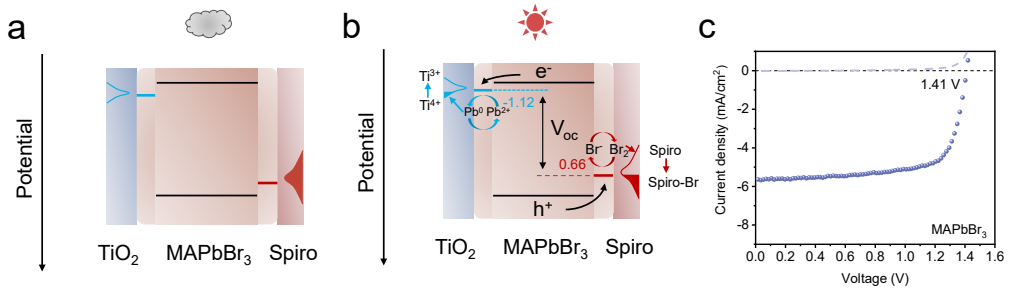

205

206 Figure S32. (a) A schematic diagram of the bulk band positions of $MAPbBr_3$ and surface
207 electrochemical potentials of $MAPbBr_3$, TiO_2, and Spiro-OMeTAD in the dark; (b) a
208 schematic diagram of interface charge transfer in TiO_2/$MAPbBr_3$/Spiro-OMeTAD
209 under illumination; (c) current-voltage curves of FTO/TiO_2/$MAPbBr_3$/Spiro-
210 OMeTAD/Au in the dark and under illumination.

211

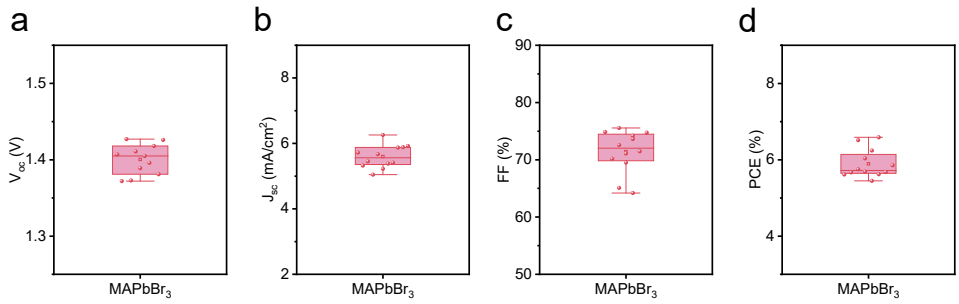

212

213 Figure S33. Statistics of V_{OC} (a), J_{SC} (b), FF (c) and PCE (d) of $MAPbBr_3$ solar cells.

214

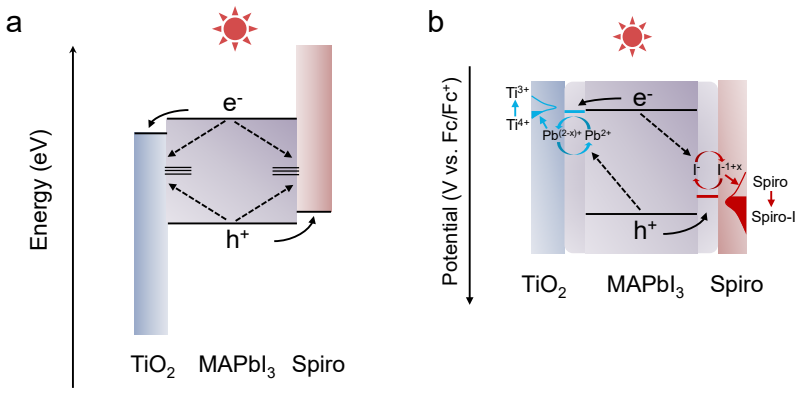

215

216 Figure S34: Different recombination processes of photo-generated carriers in
217 perovskite solar cells by energy band alignment theory (a) and faradaic junction model
218 (b).

219

The V_{OC} loss also comes from recombination processes of photo-generated carriers, which are different by energy band alignment theory and faradaic junction model (Figure S34). By energy band alignment theory, surface physical recombination happens in perovskites (Figure S34a)[2]. In contrast, by faradaic junction model, recombination processes are back chemical reactions, such as $I^{-1+x} + xe^- \rightarrow I^-$ (or $Br^{-1+x} + e^- \rightarrow Br^-$) at $MAPbI_3$ ($MAPbBr_3$)/Spiro-OMeTAD interface and $Pb^{(2-x)+} + xh^+ \rightarrow Pb^{2+}$ at $MAPbI_3$ ($MAPbBr_3$)/TiO_2 interface (Figure S34b). V_{OC} can be improved by suppressing the back chemical reactions[3]. Therefore, the difference between our experimental values and the theoretical values of V_{OC} by faradic junction model possibly comes from slow interface charge transfer rate and back chemical reactions.

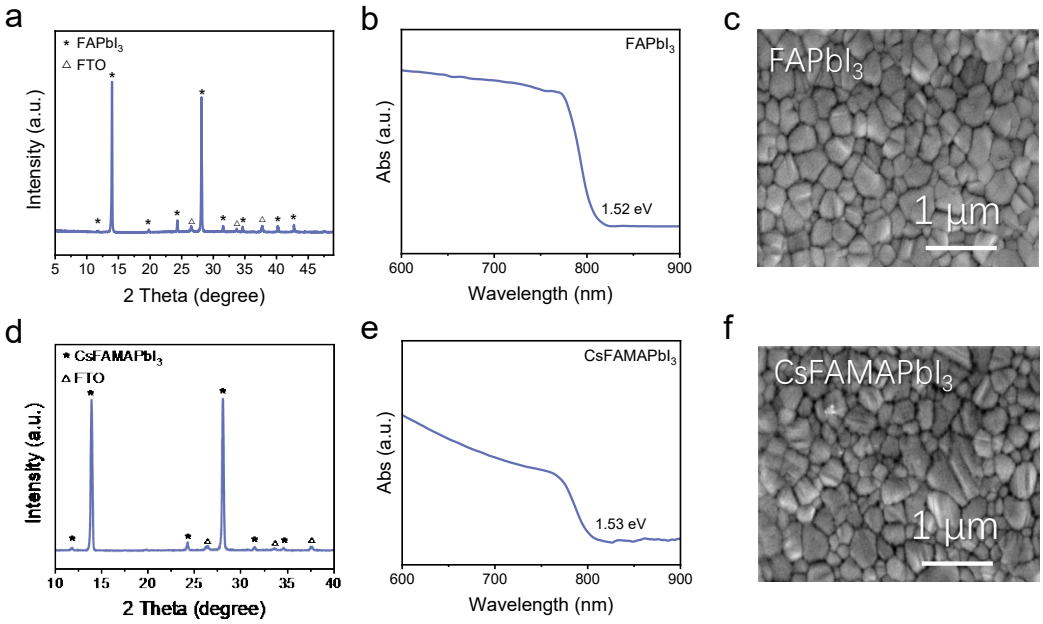

Figure S35. The XRD pattern (a), UV-vis spectra (b) and SEM image (c) of $FAPbI_3$; the XRD pattern (d), UV-vis spectra (e) and SEM image (f) of $CsFAMAPbI_3$.

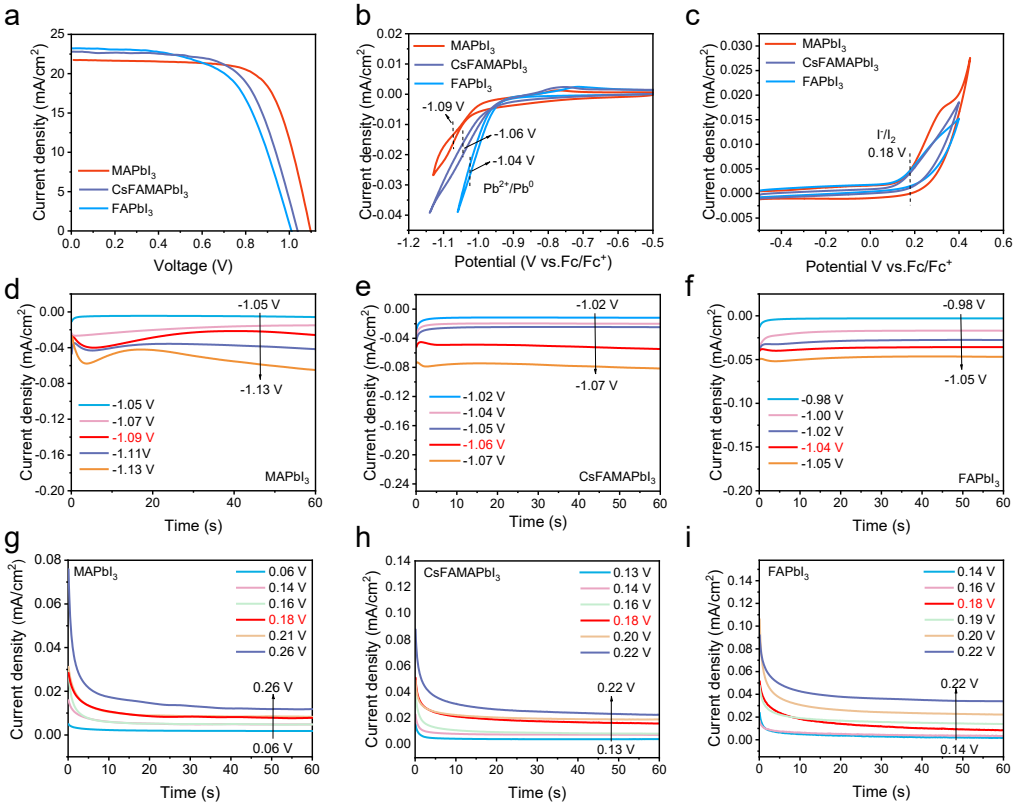

234

235 Figure S36. (a) Current-voltage curves $MAPbI_3$, $CsFAMAPbI_3$ and $FAPbI_3$ solar cells
236 in the dark and under illumination; cyclic voltammetry (CV) curves of reduction
237 reactions (b) and oxidation reactions (c) of $MAPbI_3$, $CsFAMAPbI_3$ and $FAPbI_3$; i-t
238 curves of $MAPbI_3$ (d), $CsFAMAPbI_3$ (e) and $FAPbI_3$ (f) at different reduction potentials;
239 i-t curves of $MAPbI_3$ (g), $CsFAMAPbI_3$ (h) and $FAPbI_3$ (i) at different oxidation
240 potentials; 0.1 M n-Bu_4NPF_6 in CH_2Cl_2.

241

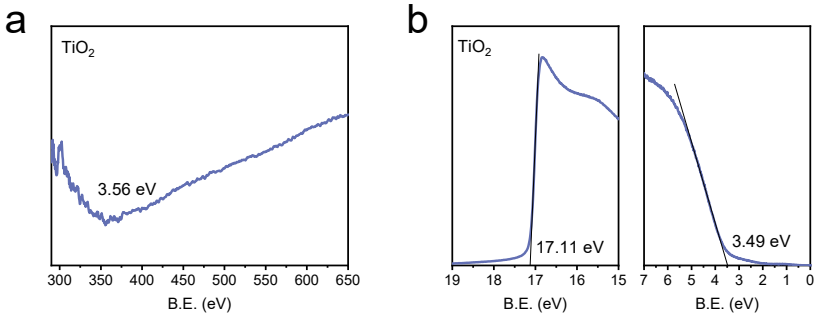

242

243 Figure S37. UV-Vis spectra (a) and UPS spectra (b) of TiO_2.

244

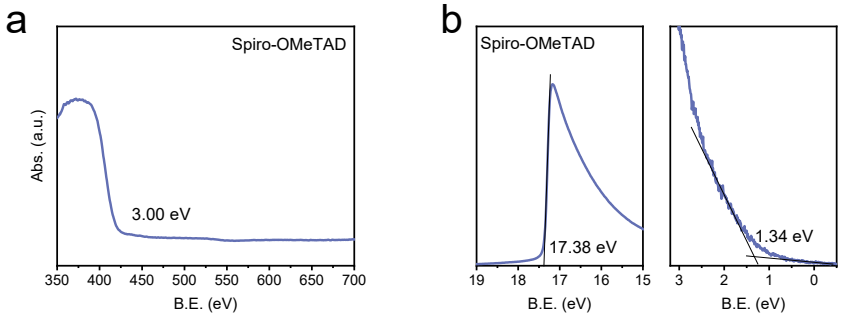

Figure S38. UV-Vis spectra (a) and UPS spectra (b) of Spiro-OMeTAD.

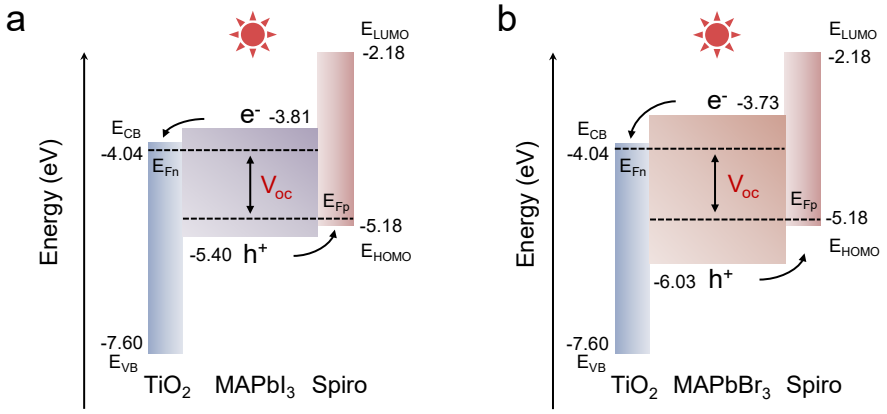

Figure S39. Schematic diagrams for interface charge transfer in a $MAPbI_3$ solar cell (a) and a $MAPbBr_3$ solar cell (b) under illumination by band alignment theory. E_{CB} and E_{VB} are the positions of conduction band and valence band; E_{LUMO} and E_{HOMO} are the positions of the lowest unoccupied molecular orbital and the highest occupied molecular orbital; E_{Fn} and E_{Fp} are the quasi-fermi level of electrons and holes.

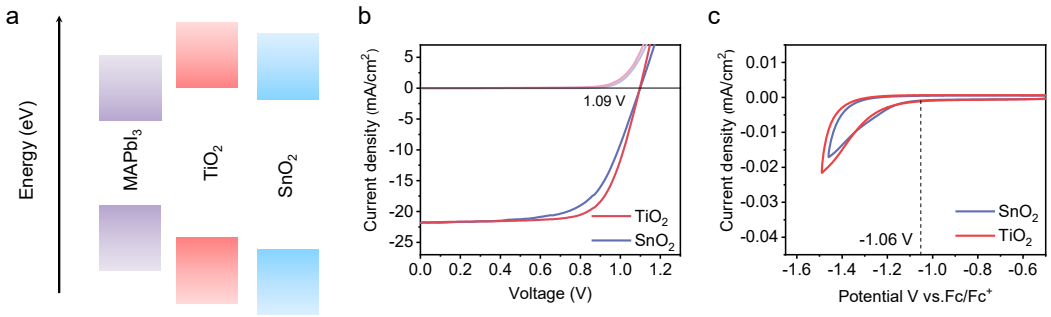

Figure S40. (a) Schematic diagrams of the conduction band and valence band of $MAPbI_3$, TiO_2 and SnO_2; (b) current-voltage curves of FTO/TiO_2/$MAPbI_3$/Spiro-OMeTAD/Au and FTO/SnO_2/$MAPbI_3$/Spiro-OMeTAD/Au in the dark and under

illumination; (c) CV curves of reduction reactions of TiO_2 and SnO_2, electrolyte: 0.1 M n-Bu_4NPF_6 in CH_2Cl_2.

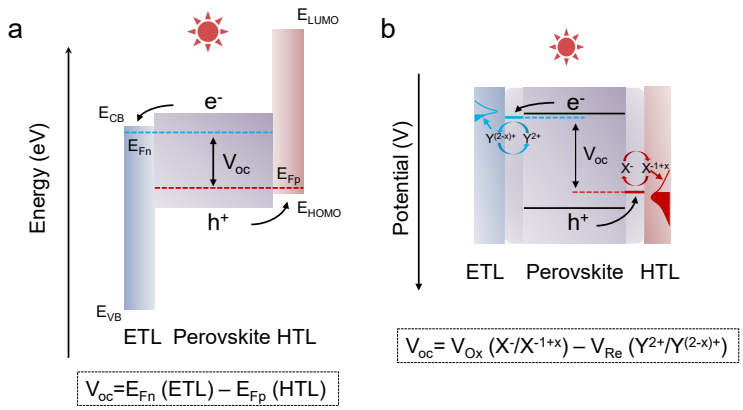

Figure S41. Schematic diagrams for the origin of V_{OC} in perovskite solar cells by energy band alignment theory (a) and electrode potential theory in faradaic junction model (b); E_{CB} and E_{VB} are the positions of conduction band and valence band; E_{Fn} and E_{Fp} are the quasi-fermi level of electrons and holes. V_{Ox} and V_{Re} are the oxidation and reduction electrode potentials.

References

1. Stamplecoskie, K. G., Manser, J. S. & Kamat, P. V. Dual nature of the excited state in organic–inorganic lead halide perovskites. *Energy Environ. Sci.* **8**, 208-215, (2015).
2. Yang, W. et al. Unlocking voltage potentials of mixed-halide perovskite solar cells via phase segregation suppression. *Adv. Funct. Mater.* **32**, 2110698, (2021).
3. Cao, D. et al. Cathodic shift of onset potential for water oxidation on a Ti^{4+} doped Fe_2O_3 photoanode by suppressing the back reaction. *Energy Environ. Sci.* **7**, 752-759, (2014).